RESEARCH ARTICLE

ADVANCED OPTICAL MATERIALS
www.advopticalmat.de

Single-Emitter White OLEDs via Microcavity Spectral Engineering

*Manish Kumar, Arpan Dutta, Hassan A. Qureshi, Michael A. Papachatzakis, Ahmed Gaber Abdelmagid, and Konstantinos S. Daskalakis**

White organic light-emitting diodes (WOLEDs) are promising candidates for next-generation lighting and display technologies. However, conventional WOLED fabrication often relies on complex doping schemes or multiple color stacked emitting layers, complicating device design, and fabrication. Here, a simple approach for fabricating ITO-free WOLEDs with a single-component, using a planar aluminium microcavity, is presented. By engineering the cavity and surface plasmon polariton modes around the emission resonance of the high-efficiency blue thermally activated delayed fluorescence emitter DMAC-DPS, electroluminescence that is spectrally broadened to white light, with a tunable color temperature ranging from 3790 to 5050 K, is achieved. The WOLEDs are top-emitting and reach an external quantum efficiency of >5%. The results are supported by optical simulations and transient emission measurements, providing insights into the emission kinetics.

1. Introduction

Organic light-emitting diodes (OLEDs) have revolutionized display technologies owing to their wide color gamut and suitability for low-energy fabrication methods on large-area and flexible substrates.[1] These advantages also make OLEDs attractive for solid-state lighting, leading to the development of white OLEDs (WOLEDs). However, the widespread adoption of WOLEDs is hindered by competition with LED counterparts for three key reasons: a) their brightness and operational lifetime are relatively low; b) their architecture requires transparent electrodes, which either involve additional processing steps[2,3] or rely on non-sustainable materials like indium tin oxide (ITO); and c) achieving white emission mainly relies on combination of red, green, and blue emitters that are either stacked as separate layers or blended in a single emitting layer.[4–9] This approach complicates the fabrication of WOLEDs as it requires precise control over emitter concentrations to maintain a balanced white spectrum, and often leads to color instability over time due to the different aging rates of the emitters.[10]

The latter challenges can be addressed by engineering the WOLED emissive layer to exhibit broadband white electroluminescence using a single type of emitter, known as single-component WOLED. Generally, this is achieved through the molecular design of emitters that exhibit emission at multiple resonances, facilitating the formation of bimolecular excitonic species[11] or display aggregation-induced emission.[12,13] However, such emitters are complex to design and synthesize, and only a few efficient single-component WOLEDs have been reported.[11,14–16] Despite these challenges, hot-exciton engineering and dual TADF emission are promising approaches.[17]

Recently, we demonstrated that a fluorescent, single-component, blue-emitting OLED can be converted to WOLED by coupling its emission to the Bragg modes of a dielectric distributed Bragg reflector (DBR).[18] Bragg modes allowed the desired wavelengths to be selected with resonance at blue, green and red, and concentrate the electric field in the emissive layer without increasing cavity thickness, while, the reflectivity stopband of the DBR was used for suppressing emission in the blue. While numerous reports exist that utilize photonic architectures such as optical microcavities and surface plasmon polaritons (SPP) for improving the performance, color rendering and operational lifetime of WOLEDs,[19–25] they are only compatible with multi-component emitting layers, unlike our previous report.[18] However, a trade-off of our previous work[18] is that the device efficiency was low (EQE < 0.1%) and DBR fabrication is generally costly and energy-intensive.[26,27]

In this work, we present a novel yet simple design for single-component WOLED using a neat film of 10,10-(4,4-Sulfonylbis(4,1 phenylene))bis(9,9-dimethyl-9,10-dihydroacridine (DMAC-DPS) as the emitting layer (EML). **Figure 1a** demonstrates our concept, which relies on an aluminium (Al)-clad microcavity with a 15-nm-thick top mirror/electrode. In this spectral engineering approach, a weak

M. Kumar, A. Dutta, H. A. Qureshi, M. A. Papachatzakis, A. G. Abdelmagid, K. S. Daskalakis
Department of Mechanical and Materials Engineering
University of Turku
Turku 20014, Finland
E-mail: konstantinos.daskalakis@utu.fi

The ORCID identification number(s) for the author(s) of this article can be found under https://doi.org/10.1002/adom.202501358

DOI: 10.1002/adom.202501358

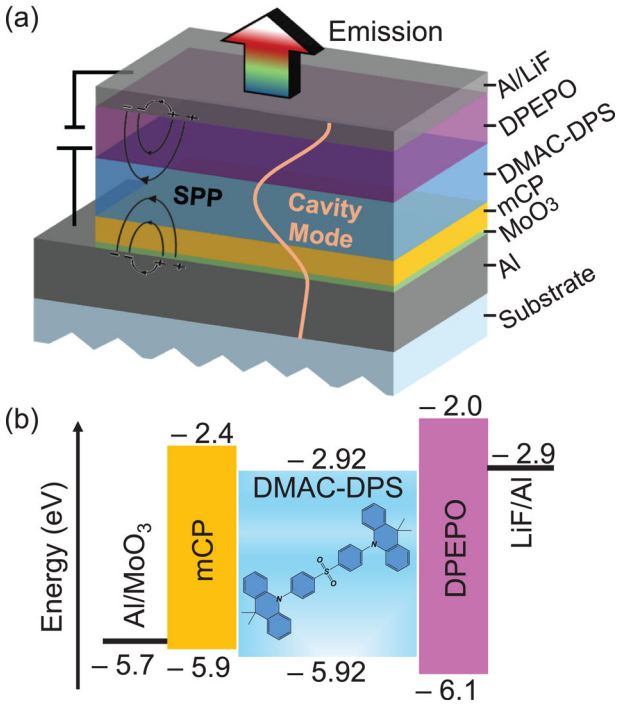

Figure 1. a) WOLED structure used in this work (from bottom to top): substrate/ Al (70 nm)/ MoO_3 (5 nm)/ mCP (40 nm)/ DMAC-DPS (d_{EML} nm)/ DPEPO (50 nm)/ LiF (1 nm)/ Al (15 nm). Here, MoO_3 was used as the hole injection layer (HIL), mCP as the hole transport layer (HTL), DMAC-DPS as the EML, DPEPO as the electron transport layer (ETL), and LiF as the electron injection layer (EIL). The Al layers work both as electrodes and cavity mirrors. The cavity mode was spectrally tuned by varying d_{EML}. The interaction between the weak cavity mode, the SPP modes at the Al/dielectric interfaces, and the DMAC-DPS emission results in a broadband white emission. b) Energy levels (HOMO and LUMO) of the WOLED layers with the chemical structure of DMAC-DPS.

cavity mode is tuned to the red tail of DMAC-DPS, redistributing its emission profile across the visible range, toward green and red, while suppressing excessive blue emission. Additionally, the thin top electrode enables surface plasmon polariton (SPP) modes at the electrode/dielectric interface to enhance the radiative rates of DMAC-DPS while minimizing power emitted lost to the evanescent SPP channel.[28] In addition, as shown in **Figure 2**, by simply increasing the effective optical cavity thickness, we can tune the emission color temperature from warm sunlight-like white to cool white (3790 to 5050K) within an emission cone of >±40 degrees (Figure 5). An optimized DMAC-DPS non-cavity OLED, which we refer to as the reference device, achieves an external quantum efficiency (EQE) of >17% and brightness of 3600 cd m^{-2}, consistent with prior reports.[29,30] Using our approach, we demonstrate WOLEDs with EQE of >5% and brightness of >1000 cd m^{-2}, with nearly 50% of the total photon flux exhibiting angle-independent white spectrum. While our method trades off the maximum achievable EQE and brightness compared to conventional transparent OLEDs, it significantly simplifies WOLED fabrication and eliminates the need of scarce ITO, making it highly attractive for large-scale production.

2. Results and Discussion

Figure 1 presents the energy level diagram and layer architecture of the DMAC-DPS OLED stack used in this study. DMAC-DPS was selected as the emitting material due to its thermally activated delayed fluorescence (TADF) character,[31,32] enabling an internal quantum efficiency (IQE) close to 100%.[29] It exhibits a broad photoluminescence spectrum ranging from 420 to 650 nm, with a dominant peak at 488 nm, classifying it as a blue emitter, which is a critical requirement for our WOLED concept. The photoluminescence (PL) spectrum of DMAC-DPS is shown in Figure S1 (Supporting Information). Additionally, DMAC-DPS single-component blue bottom-emitting OLEDs can reach EQE of nearly 20%,[29,30] making this an optimal material choice for our WOLED scheme.

In this study we designed all the WOLED (OLED) devices as top-emitting OLEDs (TEOLEDs) to achieve optimal light outcoupling. They consisting of the following layers (from bottom to top): substrate/ Al (70 nm)/ MoO_3 (5 nm)/ mCP (40 nm)/ DMAC-DPS (d_{EML} nm)/ DPEPO (50 nm)/ LiF (1 nm)/ Al (15 nm), where mCP stands for 1,3 Di(9H-carbazol-9-yl)benzene, DMAC-DPS for 10,10-(4,4-Sulfonylbis(4,1 phenylene))bis(9,9-dimethyl-9,10-dihydroacridine, and DPEPO for Bis[2(diphenylphosphino)phenyl]ether oxide. In such TEOLED geometry, the thick (70 nm) Al anode serves as a highly reflective bottom mirror, while the thin (15 nm) Al cathode was used as a leaky top mirror to form the cavity. Note that the reference OLEDs of this study share the same architecture as WOLEDs and TEOLEDs. However, they are bottom-emitting, with their anode replaced by transparent ITO (110 nm) and their cathode by a 100-nm-thick Al layer, making them identical to those reported by Zhang et al.[30] We found that in these reference OLED devices we could increase the thickness of the d_{EML} to 65 nm, which is 35 nm thicker than the previous reports,[30] while still maintaining the same electrical performance and electroluminescence, as shown in Figure S2 (Supporting Information).

By combining the EQE-optimized DMAC-DPS device architectures reported by Zhang et al.[30] (d_{EML} = 30 nm) with our TEOLED microcavity design, we obtain blue narrow electroluminescence at normal incidence, centered at 500 nm (blue), with a full-width at half-maximum (FWHM) of 40 and a maximum EQE of 14%. Further increasing d_{EML} to 45 nm resulted in 555 nm (green) emission with 51 nm FWHM and EQE 10% (Figures S2 and S3, Supporting Information).

Upon tuning the cavity mode beyond 600 nm into the deeper red region of the DMAC-DPS emission spectrum, the devices generate broad white electroluminescence shown in Figure 2a. This was accomplished in devices with d_{EML} 55 and 75 nm, yielding spectra that resemble warm white (Warm), and cool white (Cool), respectively. In particular, the electroluminescence of Warm WOLED exhibits a FWHM of 90 nm with Commission Internationale de LEclairage (CIE1931) coordinates of (0.42, 0.49) and a correlated color temperature (CCT) of 3790 K. The Cool WOLED electroluminescence displays a FWHM of 190 nm with CIE1931 coordinates of (0.38, 0.46) and a CCT of 4440 K. All WOLEDs show an uniform emission intensity across the entire visible spectrum, with the Warm and Cool WOLEDs demonstrating dominant emission peaks at ≈600 and

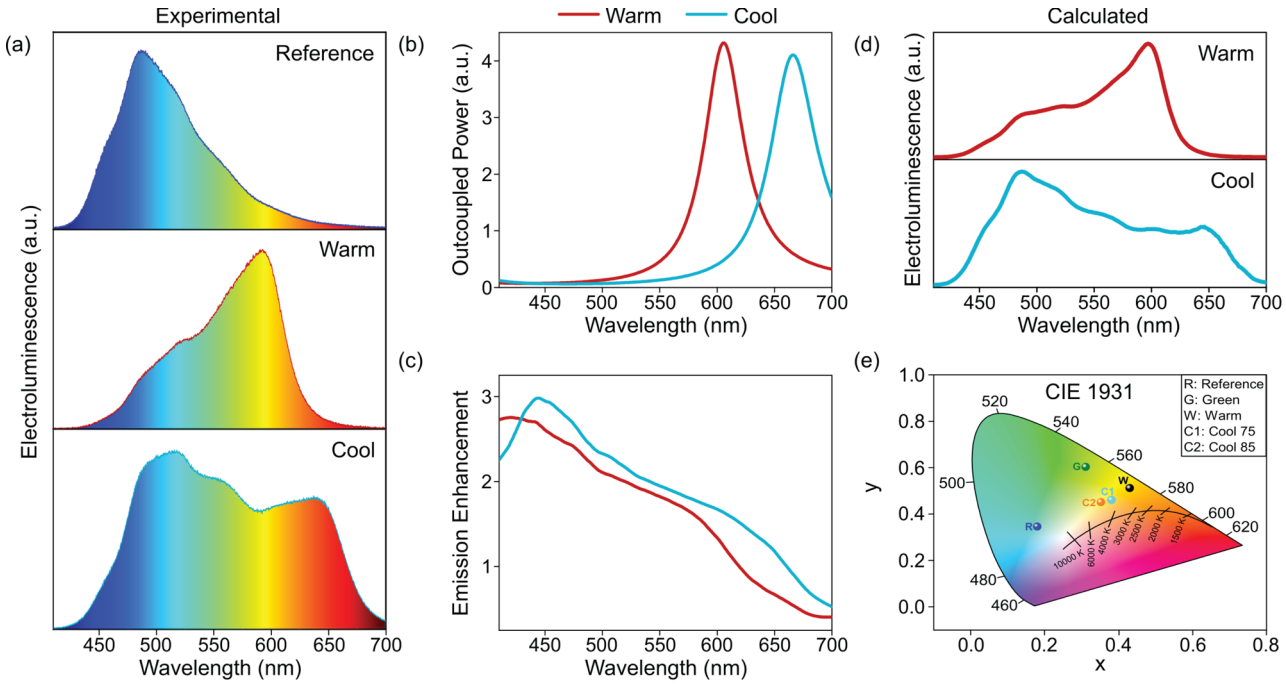

Figure 2. a) Experimental electroluminescence (EL) spectra (normalized) of the reference BEOLED and the WOLEDs: Warm (d_{EML} = 55 nm) and Cool (d_{EML} = 75 nm). Simulated b) outcoupled power spectra $P_{out}(\lambda)$ and c) emission enhancement profiles $EF(\lambda)$ of the WOLEDs. d) Calculated EL spectra (normalized) of the top-emitting WOLEDs $T_{EL}(\lambda)$ computed as $T_{EL}(\lambda) = EF(\lambda) \times P_{out}(\lambda) \times B_{EL}(\lambda)$, where $B_{EL}(\lambda)$ is the measured and normalized EL spectrum of the reference BEOLED reported in (a). e) CIE1931 coordinates and color temperatures of the reference, Green, Warm, and Cool (d_{EML} as 75 and 85 nm) OLEDs, at 0 degrees.

≈520 nm, respectively. Further increase in DMAC-DPS thickness to 85 nm (Cool-2 WOLED) results in Cool white emission (Figure S4, Supporting Information) that has CIE1931 coordinates of (0.35, 0.45) and a CCT of 5050 K. Figure 2e shows the CIE1931 map of all the OLEDs studied in this work and Figure S5 (Supporting Information) shows photographs of all the studied OLEDs.

As we demonstrate below, in a blue OLED with inherently broad emission spectrum, we achieved white electroluminescence spectrum by balancing filtering through the cavity mode, transmission losses from the top 15-nm-thick Al electrode, and radiative enhancement due to the combined effects of the cavity mode and SPPs at the electrode/dielectric interfaces within the WOLED (TEOLED).

To validate the origin of the white electroluminescence spectra, optical responses of the fabricated TEOLEDs and WOLEDs were simulated using the classical dipole model[33] combined with the transfer-matrix method for multilayer structures.[34] Figure 2b (Figure S3b, Supporting Information) depicts the simulated outcoupled power spectra ($P_{out}(\lambda)$) for the Warm and Cool WOLEDs (Blue and Green TEOLEDs). $P_{out}(\lambda)$ shows the spectral profile of the outcoupled light allowed to escape in air at 0 degrees due to the cavity mode (see Figure S8, Supporting Information). Usually in OLEDs with a well-defined microcavity mode, the main goal is to spectrally tune the cavity mode at the EML emission resonance to attain maximum Purcell enhancement.[35,36] This is the scenario that we followed for the Blue and Green TEOLEDs (see Supporting Information). For the WOLEDs, we detune the cavity mode away from the resonance of the EML emission, forcing the cavity to mainly act as a filter, thereby redistributing the emission to the targeted wavelengths.[24,25] Moreover, our low-Q (Q factor: ≈9 − 13) microcavity design having a thin top mirror yields broad cavity modes essential to convert a narrow blue emission into a broad white one. This is represented in our modeling by $P_{out}(\lambda)$ which shows a spectral red shift with an increase in d_{EML}, following the cavity resonance condition $L_c = m\lambda/2$ where L_c is the cavity length and integer m is the cavity mode number.

In our TEOLEDs and WOLEDs, along with the cavity mode, we also have SPP modes (≈400–450 nm) residing at the Al/dielectric interfaces of our devices, as schematically shown in Figure 1a. In such a scenario, the cavity mode and the SPP modes can both contribute in enhancing emission rates of the EML.[24] Figure 2c (Figure S3c, Supporting Information) shows the simulated emission enhancement profile $EF(\lambda)$ of the Warm and Cool WOLEDs (Blue and Green TEOLEDs), calculated as the ratio of the total emitted dipole power of the WOLED (TEOLED) and the BEOLED with identical EML thickness. Figure 2c shows that the emitted dipole power in our TEOLEDs and WOLEDs is higher than the equivalent BEOLEDs since $EF(\lambda) > 1$ in almost the entire visible spectrum but this enhancement washes out at larger wavelengths. In addition, contribution from both the cavity and the SPP modes is apparent since in $EF(\lambda)$, the main peak ≈450 nm originates from the SPP modes at Al/dielectric interfaces and a shoulder peak ≈600–650 nm from the cavity mode. As d_{EML} increases, the cavity mode shifts toward higher wavelengths, incurring a spectral red shift in $EF(\lambda)$ along with a slight increase in the enhancement.

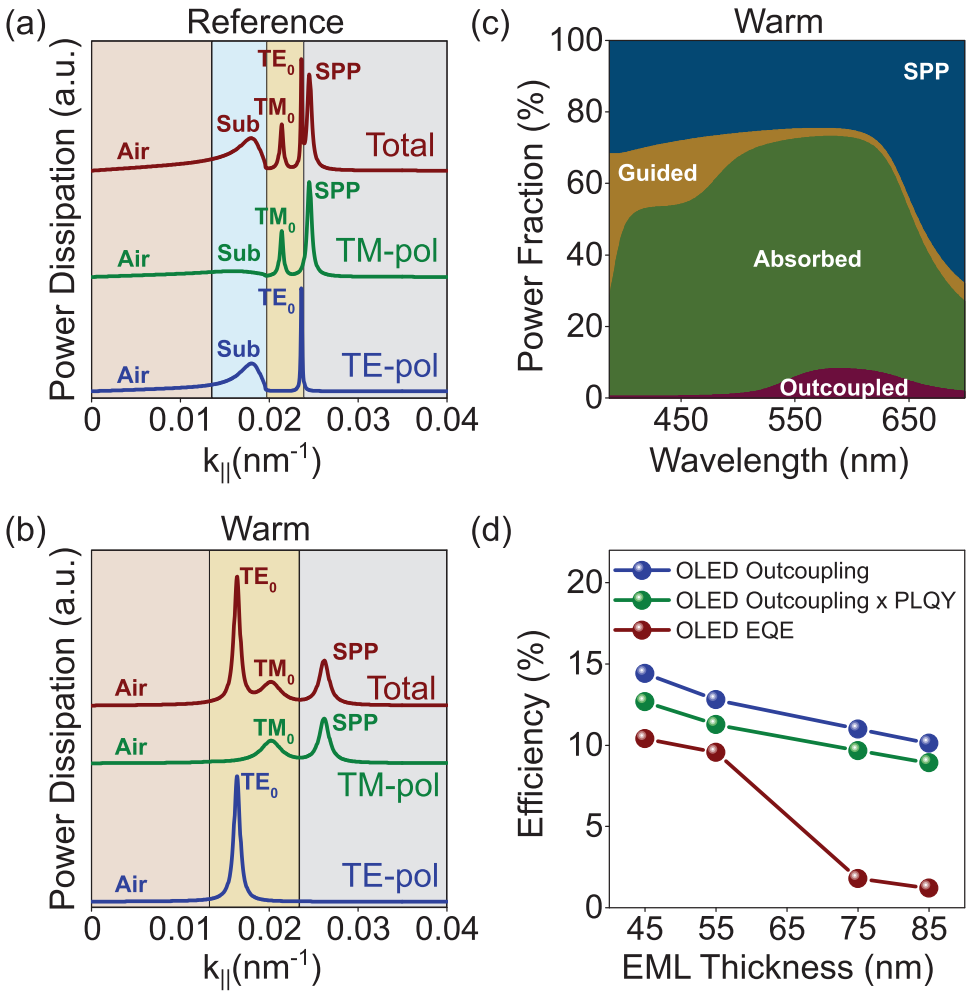

Figure 3. Dissipation of power emitted at the PL peak of DMAC-DPS (488 nm) in different optical modes as a function of in-plane wavevector ($k_{||}$) for the a) reference BEOLED and b) Warm WOLED. c) Fraction of power distributed in different optical loss channels as a function of wavelength for the Warm WOLED. d) Outcoupling efficiency (blue), theoretical EQE (green), and experimental EQE (red) as a function of EML thickness. The theoretical EQE values are estimated as outcoupling×PLQY with PLQY of DMAC-DPS as 0.88.

The DMAC-DPS electroluminescence without any cavity environment is our reference BEOLED emission $B_{EL}(\lambda)$ (Figure 2a). In the presence of a cavity, this emission is enhanced by $EF(\lambda)$ (Figure 2c) inside the OLED due to the cavity and SPP modes, i.e., the emission becomes $B_{EL}(\lambda) \times EF(\lambda)$. When outcoupled to air through the cavity, this enhanced emission is filtered, i.e., spectrally modified by the cavity mode $P_{out}(\lambda)$ (Figure 2b) resulting in an emission profile $B_{EL}(\lambda) \times EF(\lambda) \times P_{out}(\lambda)$.

Therefore, we can reconstruct the TEOLED and WOLED electroluminescence spectra $T_{EL}(\lambda)$ by simply modifying the reference BEOLED electroluminescence $B_{EL}(\lambda)$ as $T_{EL}(\lambda) = EF(\lambda) \times P_{out}(\lambda) \times B_{EL}(\lambda)$. Figure 2d shows the calculated $T_{EL}(\lambda)$ for the Warm and Cool WOLEDs showing an excellent agreement with the corresponding experimental electroluminescence spectra (Figure 2a). Figure S3 (Supporting Information) shows how the same effects persist in Blue and Green TEOLEDs, where their spectrum can also be reconstructed using the reference BEOLED.

As we see in Figure 2, as d_{EML} increases from Warm (55 nm) to Cool (75 nm), $P_{out}(\lambda)$ red shifts, spectral overlap between $B_{EL}(\lambda)$ and $P_{out}(\lambda)$ decreases, and the red part of $B_{EL}(\lambda)$ reduces. But, at the same time, with an increase in d_{EML}, $EF(\lambda)$ increases with a slight red shift which lifts up the blue-green part of $B_{EL}(\lambda)$. As a combined effect, the warm white emission changes to a cool white one.

To identify the possible optical loss channels, we performed the optical mode analysis for our BEOLED and TEOLEDs using the same transfer-matrix based classical dipole model.[33,34] **Figure 3a** shows how the power emitted at the PL peak of DMAC (488 nm) is dissipated in different optical modes as a function of in-plane wavevector ($k_{||}$) for the reference BEOLED, while Figure 3b depicts the same for the Warm WOLED. As shown in Figure 3a, in the reference BEOLED, a part of the emission outcouples to air, a part is waveguided inside the substrate (sub) and the organic layers (TE_0 and TM_0 modes), while the rest of the emission interacts with the SPP mode. In the Warm WOLED (Figure 3b), the scenario is the same, except now there is no

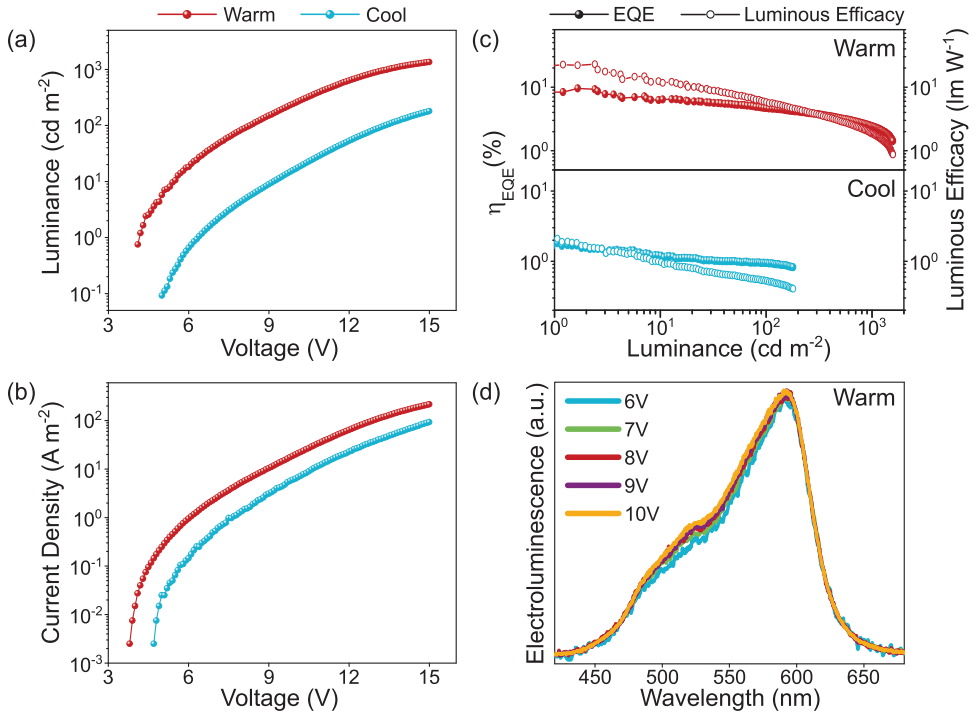

Figure 4. Performance of the Warm (d_{EML} = 55 nm) and Cool (d_{EML} = 75 nm) WOLEDs. a) Luminance and b) current density as a function of applied voltage. c) External quantum efficiency η_{EQE} (filled circles) and luminous efficacy (empty circles) as a function of luminance. d) Voltage-dependent electroluminescence spectra (normalized) of the Warm WOLED.

substrate (sub) mode present due to the non-transparent thick (70 nm) Al mirror at the bottom.

We calculated the fraction of power distributed in different optical loss channels as a function of wavelength for the Warm WOLED as reported in Figure 3c. It shows that in addition to the outcoupled (air), guided (TE_0 and TM_0), and SPP modes, there is a strong absorption in the WOLEDs. In other words, only a small fraction (10 – 15%) of the emission from our TEOLEDs and WOLEDs can outcouple to air, while the majority of the emission is either trapped or absorbed inside. This absorption loss is due to the metallic absorption of the top 15-nm-thick Al mirror/electrode (see Figure S6, Supporting Information) and it is the dominant optical loss limiting the device efficiency. Optical losses can be reduced by minimizing absorption in the electrodes. For instance, the thickness of the top aluminum electrode can be carefully decreased to lower absorption, provided this does not significantly increase resistive losses. Similarly, increasing the distance between the EML and the bottom electrode can mitigate SPP losses, as long as recombination remains unaffected. Finally, structuring the top aluminum electrode may further enhance outcoupling from SPP modes.

To estimate the upper boundary of the EQE of the WOLEDs and cavity TEOLEDs, we utilize our optical modeling approach. In our calculations, we considered a balanced charge injection, unit exciton generation for TADF emitters, the photoluminescence quantum yield (PLQY) of DMAC-DPS as 0.88,[30] and the theoretical EQE as outcoupling×PLQY. Figure 3d shows the theoretical EQE trend as a function of d_{EML} along with the experimentally measured maximum EQE, which is presented later in **Figure 4** and Figure S2 (Supporting Information). Both simulated and measured EQE drop with an increase in d_{EML}. That is because, in our TEOLEDs and WOLEDs, as the cavity thickness (d_{EML}) increases, the cavity mode red shifts (Figure 2b and Figure S3b, Supporting Information). As a result, the detuning between the cavity mode and the EML emission increases, resulting in a poor spectral overlap.

In addition, Figure 3d shows that the experimental EQE is lower than the theoretical values, with the discrepancy becoming more pronounced for thicker cavities (d_{EML} > 55 nm). This is because the theoretical EQE values are calculated under the assumption of an OLED with balanced charge injection. However, in practice, replacing ITO with Al can lead to charge imbalance, and increasing d_{EML} shifts the recombination zone away from the optimal position within the EML. This, in turn, causes an imbalanced charge transport and increased exciton quenching. To validate this, we performed recombination zone profile simulations for the BEOLED (65 nm), thick BEOLED (85 nm), TEOLED (warm 55 nm), and TEOLED (cool 85 nm) and confirmed the shift of the recombination zone toward the EML/ETL interface in TEOLEDs, shown in Figure S13 (Supporting Information). Furthermore, we fabricated the BEOLED with a thicker DMAC-DPS (85 nm), and this resulted in a lower EQE of 13.9% than the 17.6% of the reference device (Figure S12c, Supporting Information), which further confirms that the EQE also drops in BE devices with a thick 85 nm EML. Figure 4 (Figure S2, Supporting Information) reports the luminance and current density as a function of applied voltage, while the EQE and luminous efficacy as a function of luminance, for the WOLEDs (reference BEOLED and TEOLEDs). As shown in Figure 4, the warm WOLED

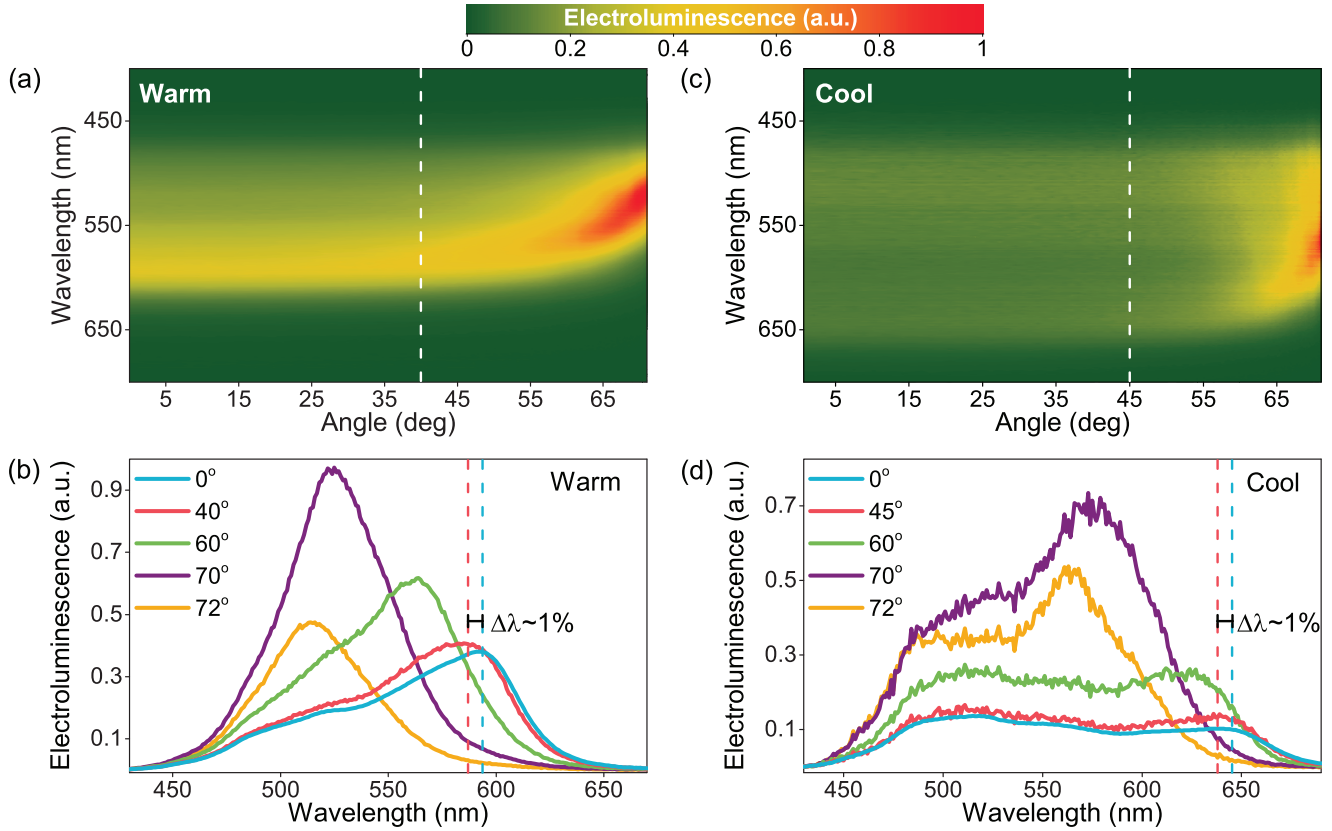

Figure 5. Contour plots of angle-resolved electroluminescence (normalized) for the a) Warm and c) Cool WOLEDs. The dashed white lines show the angles at which spectral shift ($\Delta\lambda$) reaches 1%. Angle-dependent electroluminescence spectra (normalized) of the b) Warm and d) Cool WOLEDs. The dashed red and blue lines show the spectral peak positions used to define the 1% spectral shift ($\Delta\lambda$).

exhibited turn-on voltage (V_{on} at 1 cd m^{-2}) at 4.4 V, while a thicker EML (cool WOLED) results in a higher turn-on voltage of 6.3 V, indicating increased resistive losses and less favorable charge recombination dynamics. The current density of cool WOLED is lower than that of warm WOLED, mainly due to the thick emissive layer. The warm WOLED showed L_{max} of 1580 cd m^{-2}, η_{EQE} of 4.7% and η_{PE} of 6% at 100 cd m^{-2}. The cool WOLED exhibited L_{max} of 180 cd m^{-2}, η_{EQE} of 1%, and η_{PE} of 0.5% at 100 cd m^{-2}.

To confirm spectral stability, voltage-dependent EL spectra and corresponding CIE (x, y) coordinates were measured for all devices (summarized in Figure 4d; Figure S9 and Table S1, Supporting Information). Interestingly, Figure 4d shows that the WOLED emission spectrum remains stable even as the driving voltage increases, despite the substantial efficiency roll-off observed in Figure 4c. This stability is an advantageous feature of our single-component WOLED scheme, as it does not rely on balancing the emission intensities of multiple states or emitting layers. In contrast, in stacked emissive layer WOLEDs, changes in bias voltage can disproportionately enhance emission from a single layer. Similarly, in WOLEDs that rely on bimolecular excitonic species, high electrical excitation modifies the potential landscape between molecular species, leading to a voltage-dependent color shift.[18] Retrospectively, the color stability in our WOLEDs confirms that no exciplex or excimer-type emissions are contributing to the broad white emission. Note also here that the HOMO-LUMO energy levels of DPEPO (HOMO: 6.1 eV, LUMO: 2.0 eV) and DMAC-DPS (HOMO: 5.92 eV, LUMO: 2.92 eV) do not energetically favour the exciplex formation at the DMAC-DPS/DPEPO interface. For exciplex formation, the charge transfer state would typically be at an energy lower than the individual frontier molecular orbitals of the donor and acceptor, but in this case, the large energy gap between the LUMO levels and the relatively close HOMO levels makes charge transfer inefficient.[37] Since no new low-energy emission features are observed in the case of BEOLED and the observed emission is consistent with the previously reported DMAC-DPS blue OLEDs,[29,30] we can rule out the possibility of excimer formation.

To evaluate the operational stability of the devices, we performed lifetime measurements for both the reference BEOLED and the top-emitting warm WOLED at an initial luminance of 200 cd m^{-2}. As shown in Supplementary Figure S10 (Supporting Information), the reference BEOLED exhibited an LT_{50} of 9 min, while the warm WOLED showed an LT_{50} of 3 min. The reduced operational stability is attributed to the intrinsic instability of the DMAC-DPS emitter.[29]

Figure 5a,c shows contour plots of the angle-resolved electroluminescence for the Warm and Cool WOLEDs, respectively. In both WOLEDs, strong cavity dispersion appears only at emission angles above 40 and 45 degrees for Warm and Cool WOLEDs, respectively. Interestingly, within the emission cone corresponding to white light, the WOLEDs exhibit only a negligible spectral shift

(<1%). At higher angles, however, the electroluminescence spectrum shifts back toward blue, while the intensity increases rapidly (Figure 5b,d). From these emission maps, we calculated the fraction of the total photon flux that lies within the white emission cone, as shown in Figure S7 (Supporting Information). For both the Warm and Cool WOLEDs, we find that ≈50% of the total photon flux falls within the white light region. To quantify the angular color stability of the devices, we calculated the CIE 1931 (x, y) coordinates at various viewing angles for both the warm (55 nm) and cool (85 nm) WOLEDs. As shown in Table S2 (Supporting Information), the change in color coordinates from 0 to 40 degrees for the warm WOLED is approximately ΔCIE ($x \approx 2.38\%$, $y \approx 2.04\%$). Similarly, for the cool WOLED, the variation from 0 to 50 degrees remains within ΔCIE ($x \approx 2.86\%$, $y \approx 2.22\%$). These values confirm that both devices exhibit relatively stable emission across a wide range of viewing angles, with minimal chromaticity drift.

We measured the transient photoluminescence (TRPL) decay spectra of a DMAC-DPS neat film and the Warm WOLED at room temperature, where the excitation wavelength was 370 nm and the detection was over the entire white spectrum (480–620 nm). As shown in **Figure** 6a, the prompt emission lifetime (τ_p) of the Warm WOLED ($\tau_{p1} = 17.3$ ns) is smaller than that of the DMAC-DPS neat film ($\tau_{p2} = 20.2$ ns). This shortening of the prompt lifetime can be due to the radiative enhancement of the singlet state,[35,36] in line with our theoretical prediction in Figure 2c. From the measured lifetimes, we can estimate the enhancement as τ_{p2}/τ_{p1} and for the prompt emission, it is 1.16. In agreement with our simulated enhancement rates in Figure 2c, we measured an emission enhancement of 1.8 when we selectively measured the emission lifetime at 430 nm (Figure 6c). This enchantment is lower than the simulated value (≈2.7) but the overall trend supports our simulations.

We also measured the delayed emission lifetime. As shown in Figure 6b, our Warm WOLED shows relatively small lifetime ($\tau_{d1} = 1.4$ µs) than the DMAC-DPS neat film ($\tau_{d2} = 2.4$ µs). Since the delayed emission rate is fundamentally set by the reverse intersystem crossing (RISC) rates, we attribute this to an increase in the triplet quenching rate.[38–43]

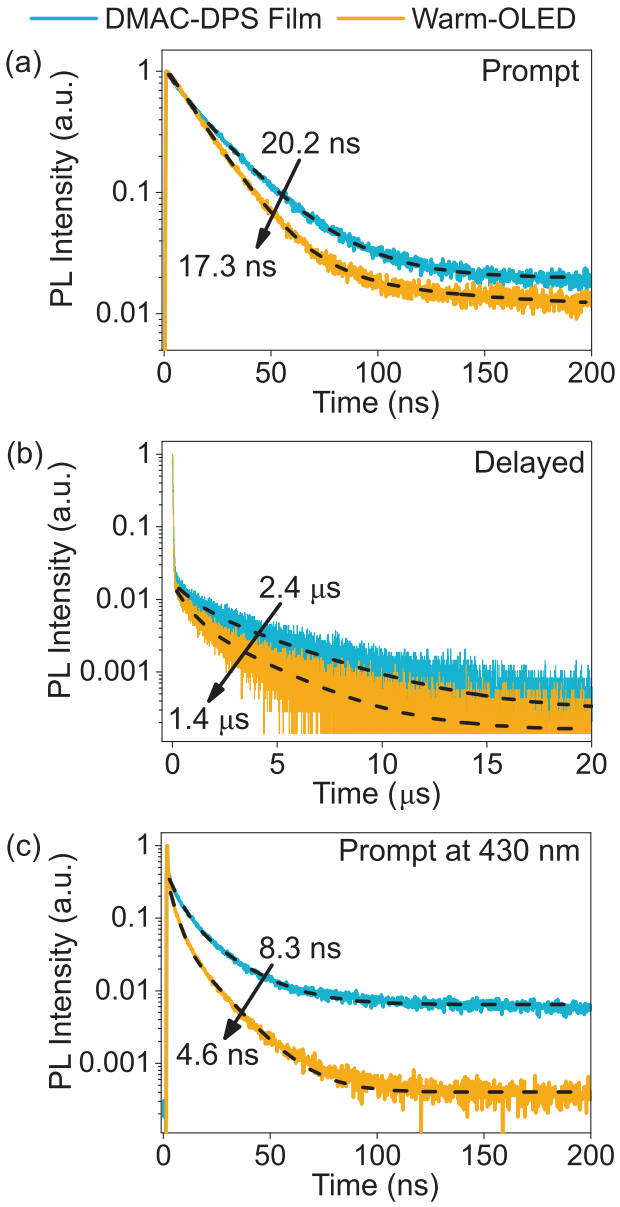

Figure 6. Transient photoluminescence (TRPL) decay characteristics of DMAC-DPS neat-film (blue) and Warm WOLED (yellow) for an excitation wavelength of 370 nm. Fluorescence lifetime of the a) prompt and b) delayed parts. The TRPL lifetime was detected over the wavelength range of 480–620 nm. c) Prompt fluorescence lifetime detected at 430 nm. The dashed lines in the figure represent the double exponential fits used to calculate the lifetimes.

3. Conclusion

In conclusion, we have demonstrated a proof-of-concept WOLED design that eliminates the need for both ITO electrodes and multi-component emitting layers, thereby significantly simplifying device fabrication. Our approach employs high-efficiency DMAC-DPS neat films as a single-component EML, with emission spectrally broadened to white light through the combined effects of SPP and cavity modes in an Al-clad microcavity structure featuring a 15-nm-thick top mirror/electrode. We show that the color temperature of the WOLEDs can be readily tuned from 3790 to 5050 K by simply increasing the EML thickness, thereby altering the effective optical thickness of the cavity. Although increased EML thickness leads to reduced device performance, this trade-off can potentially be mitigated in future designs by optimizing the thickness of the charge transport layers to enhance carrier recombination. Our experimental findings are supported by optical simulations based on a classical dipole emission model combined with the transfer-matrix method. The simulated outcoupled power spectra closely reproduce the experimental electroluminescence spectra, confirming that the observed spectral broadening and shifts originate from the engineered cavity modes and the Purcell enhancement via the cavity mode and SPPs at the Al/dielectric interface. Transient emission measurements further reveal enhanced radiative rates, as predicted by the model. However, the overall EQE, brightness, and efficiency roll-off remained below that of optimized blue reference OLEDs with transparent ITO electrodes, which we attribute to

suboptimal electrical injection and optical losses in the current design. These findings highlight the potential of photonic microcavity OLEDs for spectrally engineered lighting applications and pave the way toward cost-effective, large-scale fabrication of WOLEDs.

4. Experimental Section

OLED Fabrication: Bottom reference OLEDs were fabricated on prepatterned 15 × 15 mm^2 ITO and top-emitting cavity OLEDs were fabricated on glass substrates. Prepatterned ITO-coated glass substrates were obtained from Lumtec (resistivity 15 ohm sq^{-1}). The substrates were first ultrasonically cleaned in a 2% Dacon-90/DI water solution for 10 min. The substrates were then subsequently cleaned in DI water, acetone, and isopropanol for 10 min each and dried by nitrogen blow. Cleaned substrates were transferred to an Angstrom thermal evaporator system. For top-emitting OLEDs, a 70 nm Al anode was deposited using a shadow deposition mask. All the OLED layers (organics, Al, and dielectrics) were deposited at a base pressure of 3×10^{-7} mbar with the deposition rates: 2 Å s^{-1} (bottom Al), 0.5 Å s^{-1} (top Al), 0.1 Å s^{-1} (LiF), 0.2 Å s^{-1} (MoO_3), and 1 Å s^{-1} (DMAC-DPS, mCP, and DPEPO).

Electrical Characterization: OLEDs were measured inside a glovebox using an in-house built setup coupled with a Keysight-B2902B source meter to measure current and voltage. The photocurrent was measured from a NIST-calibrated large-area Si-photodiode (active area 10 × 10 mm^2). The photodiode was placed on top of the active pixel at a 0.1 mm distance, and the photons were captured in the forward direction. The electroluminescence was captured using Ocean Optics USB2000$^+$ at 0 degrees. The external quantum efficiency (EQE), luminance, and power efficiency were determined using the measured photocurrent, device current, and electroluminescence spectrum collected at 0 degrees.

Optical Characterization: The angle-dependent reflectivity, transmission, optical constants, and thicknesses of thin films were acquired using a J.A. Woollam VASE ellipsometer. A Xe lamp with a spectral range of 250–2500 nm was utilized to obtain the spectra. The data was analyzed by fitting a Cauchy model in the transparent region of the film to acquire optical constants and thickness.

For the angle-resolved electroluminescence, a custom-built angle-resolved imaging setup was used. The emission was collected using a microscope objective with a numerical aperture of 0.95, allowing us to collect the electroluminescence from ≈−70 to +70 degrees. The collected light was then focused into the slit of the spectrometer that was coupled to a 2D CCD camera (1340 × 400 pixels).

Optical Simulation and Modeling: To simulate optical properties of OLED, a classical dipole model[33] combined with transfer-matrix method[34] in 1D is used. The dipole model, also known as the Chance-Prock-Silbey (CPS) model, considers an electrical dipole emitting inside the OLED and the emitted light is interacting with all the interfaces present in a multilayer OLED.[33] The optical simulations are implemented in MATLAB[44] and SETFOS.[45]

Supporting Information

Supporting Information is available from the Wiley Online Library or from the author.

Acknowledgements

This project had received funding from the Research Council of Finland project "Hyper-MOLED" (Decision number 348727), the European Research Council (ERC) under the European Unions Horizon 2020 research and innovation programme (grant agreement Number 948260), and the European Innovation Council through the project SCOLED (Grant Agreement Number 101098813).

Conflict of Interest

Manish Kumar and Konstantinos S. Daskalakis are inventors of a pending patent (application number PCT/FI2024/050710) filed by the University of Turku. The other authors declare no conflict of interest.

Author Contributions

M.K. and A.D. contributed equally to this work. M.K. and K.S.D. designed and initiated the project. M.K. designed and fabricated the microcavities, optimized the OLEDs, performed majority of the experiments, and analyzed the data. A.D. performed the optical simulations and analyzed the data. H.Q. performed the TRPL lifetime and angle-resolved electroluminescence measurements. M.A.P. designed the IVL characterization setup and helped in the IVL measurements. M.K., A.D., and K.S.D. wrote the manuscript with contributions from all authors. K.S.D. supervised the project.

Data Availability Statement

The data that support the findings of this study are available from the corresponding author upon reasonable request.

Keywords

ITO-free, microcavity, single-component WOLED, TADF

Received: April 29, 2025
Revised: July 10, 2025
Published online:

[1] G. Hong, X. Gan, C. Leonhardt, Z. Zhang, J. Seibert, J. M. Busch, S. Bräse, *Adv. Mater.* **2021**, *33*, 2005630.
[2] W. Gaynor, S. Hofmann, M. G. Christoforo, C. Sachse, S. Mehra, A. Salleo, M. D. McGehee, M. C. Gather, B. Lüssem, L. Müller-Meskamp, P. Peumans, K. Leo, *Adv. Mater. (Deerfield Beach, Fla.)* **2013**, *25*, 4006.
[3] H.-W. Chang, Y. H. Kim, J. Lee, S. Hofmann, B. Lüssem, L. Müller-Meskamp, M. C. Gather, K. Leo, C.-C. Wu, *Org. Electron.* **2014**, *15*, 1028.
[4] Y. Sun, N. C. Giebink, H. Kanno, B. Ma, M. E. Thompson, S. R. Forrest, *Nature* **2006**, *440*, 908.
[5] S. Reineke, F. Lindner, G. Schwartz, N. Seidler, K. Walzer, B. Lüssem, K. Leo, *Nature* **2009**, *459*, 234.
[6] Y. Yin, M. U. Ali, W. Xie, H. Yang, H. Meng, *Mater. Chem. Front.* **2019**, *3*, 970.
[7] H. Liu, Y. Fu, B. Z. Tang, Z. Zhao, *Nat. Commun.* **2022**, *13*, 5154.
[8] C. Zhang, D. Zhang, Z. Bin, Z. Liu, Y. Zhang, H. Lee, J. H. Kwon, L. Duan, *Adv. Mater.* **2022**, *34*, 2103102.
[9] M. Huang, Z. Chen, J. Miao, S. He, W. Yang, Z. Huang, Y. Zou, S. Gong, Y. Tan, C. Yang, *Nat. Commun.* **2024**, *15*, 8048.
[10] M. C. Gather, R. Alle, H. Becker, K. Meerholz, *Adv. Mater.* **2007**, *19*, 4460.
[11] Z. Chen, C.-L. Ho, L. Wang, W.-Y. Wong, *Adv. Mater.* **2020**, *32*, 1903269.
[12] J. Zhang, Q. Wei, W. Li, H. Chen, X. Zhu, Y. Bai, N. Fei, L. Cao, Z. Zhao, A. Qin, B. Z. Tang, Z. Ge, *Aggregate* **2024**, *5*, e410.
[13] J. Chatsirisupachai, P. Nalaoh, C. Kaiyasuan, P. Chasing, T. Sudyoadsuk, V. Promarak, *Mater. Chem. Front.* **2021**, *5*, 2361.
[14] G.-X. Yang, Z. Chen, Z. Yang, D. Liu, S. Jiang, D. Li, J. Hu, M. Li, S.-J. Su, *Adv. Opt. Mater.* **2024**, *12*, 2401818.

[15] F. Liu, H. Liu, Y. Chen, X. He, Z. Cheng, X. Ma, X. Qiao, D. Ma, P. Lu, *CCS Chem*. **2025**, 1.
[16] Y.-H. Chen, K.-C. Tang, Y.-T. Chen, J.-Y. Shen, Y.-S. Wu, S.-H. Liu, C.-S. Lee, C.-H. Chen, T.-Y. Lai, S.-H. Tung, R.-J. Jeng, W.-Y. Hung, M. Jiao, C.-C. Wu, P.-T. Chou, *Chem. Sci.* **2016**, *7*, 3556.
[17] M. Liu, H. Li, H. Ma, C. Yao, F. Zhao, S. Han, Z. Zhang, N. Wang, X. Yin, *ACS Appl. Mater. Interfaces* **2025**, *17*, 21509.
[18] K. S. Daskalakis, F. Freire-Fernandez, A. J. Moilanen, S. Van Dijken, P. Torma, *ACS photonics* **2019**, *6*, 2655.
[19] C. E. Arneson, H. Zhao, S. R. Forrest, *Adv. Funct. Mater.* **2024**, *34*, 2410741.
[20] X.-L. Zhang, J. Feng, X.-C. Han, Y.-F. Liu, Q.-D. Chen, J.-F. Song, H.-B. Sun, *Optica* **2015**, *2*, 579.
[21] J. Lee, T.-W. Koh, H. Cho, S. Hofmann, S. Reineke, J.-H. Lee, J.-I. Lee, S. Yoo, K. Leo, M. C. Gather, *Org. Electron.* **2015**, *26*, 334.
[22] X. Zhang, T. Pan, J. Zhang, L. Zhang, S. Liu, W. Xie, *Acs Photonics* **2019**, *6*, 2350.
[23] S. Jeong, S. Jung, H. Kang, S.-B. Choi, S. Hong, J. Lee, K. Yu, N. Kim, S. Kee, D.-S. Lee, K. Lee, *Adv. Opt. Mater.* **2020**, *8*, 1901365.
[24] H. Zhao, C. E. Arneson, D. Fan, S. R. Forrest, *Nature* **2024**, *626*, 300.
[25] M. Wan, W. Zhu, L. Huang, Y. Zhao, Z. Wang, J. Li, B. Wei, *Org. Electron.* **2022**, *100*, 106381.
[26] E. Palo, K. S. Daskalakis, *Adv. Mater. Interfaces* **2023**, *10*, 2202206.
[27] H. A. Qureshi, M. A. Papachatzakis, A. G. Abdelmagid, M. Salomäki, E. Mäkilä, O. Tuomi, O. Siltanen, K. S. Daskalakis, *Adv. Opt. Mater.* **2025**, *13*, 2500155.
[28] Y. Bai, J. Feng, Y. F. Liu, J. F. Song, J. Simonen, Y. Jin, Q. D. Chen, J. Zi, H. B. Sun, *Org. Electron.* **2011**, *12*, 1927.
[29] Q. Zhang, B. Li, S. Huang, H. Nomura, H. Tanaka, C. Adachi, *Nat. Photonics* **2014**, *8*, 326.
[30] Q. Zhang, D. Tsang, H. Kuwabara, Y. Hatae, B. Li, T. Takahashi, S. Y. Lee, T. Yasuda, C. Adachi, *Adv. Mater. (Deerfield Beach, Fla.)* **2015**, *27*, 2096.
[31] H. Uoyama, K. Goushi, K. Shizu, H. Nomura, C. Adachi, *Nature* **2012**, *492*, 234.
[32] Y. Liu, C. Li, Z. Ren, S. Yan, M. R. Bryce, *Nat. Rev. Mater.* **2018**, *3*, 1.
[33] M. Furno, R. Meerheim, S. Hofmann, B. Lüssem, K. Leo, *Phys. Rev. B* **2012**, *85*, 115205.
[34] K. J. Pascoe, Reflectivity and transmissivity through layered, lossy media: a user-friendly approach, Technical report, Air Force Institute of Technology, Wright-Patterson Air Force Base, **2001**.
[35] K. Vahala, *Nature* **2003**, *424*, 839.
[36] A. Dutta, V. Tiainen, J. J. Toppari, *IOP SciNotes* **2021**, *2*, 015205.
[37] M. Sarma, L.-M. Chen, Y.-S. Chen, K.-T. Wong, *Mater. Sci. Eng. R: Rep.* **2022**, *150*, 100689.
[38] A. G. Abdelmagid, H. A. Qureshi, M. A. Papachatzakis, O. Siltanen, M. Kumar, A. Ashokan, S. Salman, K. Luoma, K. S. Daskalakis, *Nanophotonics* **2024**, *13*, 2565.
[39] E. Eizner, L. A. Martínez-Martínez, J. Yuen-Zhou, S. Kéna-Cohen, *Sci. Adv.* **2019**, *5*, eaax4482.
[40] C. Zang, S. Liu, M. Xu, R. Wang, C. Cao, Z. Zhu, J. Zhang, H. Wang, L. Zhang, W. Xie, C.-S. Lee, *Light: Sci. Appl.* **2021**, *10*, 116.
[41] O. Siltanen, K. Luoma, A. J. Musser, K. S. Daskalakis, *Adv. Opt. Mater.* **2025**, *13*, 2403046.
[42] O. Siltanen, K. Luoma, K. S. Daskalakis, *arXiv:2501.01800* **2025**.
[43] Y.-C. Wei, C.-H. Wang, K. S. Daskalakis, P.-T. Chou, S. Murai, J. Gómez Rivas, *ACS Photonics* **2025**, *12*, 2193.
[44] MATLAB, *version 24.1.0.2537033 (R2024a)*, The MathWorks Inc. **2024**, https://se.mathworks.com/products/matlab.html (accessed: July 2025).
[45] SETFOS, *version 5.5*, Fluxim AG **2024**, https://www.fluxim.com/setfos-intro, (accessed: July 2025).